Chapter Two: The Navier-Stokes Schemes from Gas-Kinetic Theory

2.1 Introduction

Solving the full system of the Navier-Stokes equations is the ultimate goal of a numerical flow simulation. It is generally accepted that all the properties of a continuum flow system can be described by the Navier-Stokes equations.

Most current numerical schemes for solving the Navier-Stokes equations are based largely on the methods developed for inviscid flows (which will be analyzed in detail in the next chapter), where the additional viscous and heat conductive terms are approximated by central differences. The presence of artificial dissipation terms in the discretized inviscid Euler equations can interfere with the physical dissipation represented by the real molecular and turbulent viscosity. Also, as will be mentioned in detail in the next chapter, in most real problems the mesh resolution is not fine enough to resolve the diffusive effects of viscosity and heat conduction in regions of severe gradients such as shocks. Therefore, extra artificial dissipation has to be introduced even for Navier-Stokes calculations, at least at high Reynolds numbers.

In this chapter we give an alternative numerical approach to the Navier-Stokes equations from gas-kinetic theory. As mentioned at the end of last chapter, we use the physical BGK model, instead of the original Boltzmann equation as the basis to describe the gas flow, where the connection between the collision time τ in the BGK model and viscosity coefficients in the Navier-Stokes equations is explicit. The scheme developed in this chapter is both a spatial and temporal high-resolution gas kinetic scheme, and the advective and diffusive fluxes are coupled and solved at the same time by integrating the time-dependent velocity distribution function for the particles. Numerical results for some well-defined Navier-Stokes test cases are presented. The Kolmogorov and the Laminar Boundary Layer problems verify the real viscosity effects in the scheme, and the isotropic turbulent flow test shows that this scheme is competitive with other high-resolution ENO Navier-Stokes codes.

2.2 Preliminary Gas-Kinetic Theory for the BGK Model

Our numerical code is based on the dynamical theory of gases, rather than the Euler or Navier-Stokes equations. As is well known these equations can be derived from gas dynamics, so that a solution of a problem in gas dynamics is automatically a solution of a problem in hydrodynamics if the two conditions (*cf.* Eq.(1.11)) are satisfied. In this section, we will introduce the gas dynamical BGK model and present some of its physical properties. More detailed analysis is given in paper [28].

The BGK model in three dimensional case is

$$f_{,t} + u_i f_{,i} = \frac{(g-f)}{\tau}, \tag{2.1}$$

where f is the true gas distribution function in space x_i and time t, u_i are the velocities for a single particle in the $\widehat{x_i}$ directions respectively, and g is the equilibrium state approached by f through collisions. The BGK model can be interpreted as a phenomenological description of the tendency of the real gas distribution function f under collisions to approach an equilibrium state g on a time scale τ; more specifically, along any trajectory in phase space (x_i, u_i) particles are destroyed at a rate given by τ and regenerated from the equilibrium distribution g. The relaxation time τ can be a very complicated functional of the distribution f, but for most cases, aside from the discontinuity regions, it is reasonable to regard it as a function of the local density and temperature. The connection between the macroscopic description of the gas, described by mass $\rho(\vec{x},t)$, momentum $P_i(\vec{x},t)$ and energy $\epsilon(\vec{x},t)$ densities, with the real gas distribution function $f(\vec{x},\vec{u},t)$ is

$$\begin{pmatrix} \rho \\ P_i \\ \epsilon \end{pmatrix} = \int \begin{pmatrix} 1 \\ u_i \\ \frac{1}{2}({u_k}^2+\xi^2) \end{pmatrix} f d\Xi, \tag{2.2}$$

where $d\Xi = \xi^{K-1} d\xi du_i$ and ξ is a K dimensional vector to take care of energy in internal degrees of freedom. For example, for one-dimensional flow of a perfect gas with constant ratio of specific heats, it will be convenient to treat the motion of the molecules in the direction perpendicular to the flow by adding two internal degrees of freedom to the ones required to give the correct value of γ. For a real gas in three dimensions, classical statistical mechanics gives $\gamma = (n+2)/n$, where n is the total number of "effective" degrees of freedom of the molecule: thus a monoatomic gas has $n=3$, $\gamma = 5/3$, and a diatomic gas, with two rotational degrees of freedom excited at ordinary temperatures, has $n=5$, $\gamma = 7/5$. For a flow in D dimensions, we treat D of the n degrees of freedom explicitly, and $K = -D + 2/(\gamma - 1)$. Thus for air, for example, $\gamma \simeq 7/5$, and for flow in one dimension, $K = 4$.

Since the real gas distribution function f, unlike the Maxwellian, has no generally fixed form , but depends on the particular problem, the local mass density ρ, momentum P_i and energy ϵ cannot uniquely determine f from Eq.(2.2). Owing to the conservation laws of mass, momentum and energy during particle collisions, the distribution functions of g and f in the BGK model have to satisfy the conservation constraints

$$\int \begin{pmatrix} 1 \\ u_i \\ \frac{1}{2}({u_k}^2+\xi^2) \end{pmatrix} \frac{(f-g)}{\tau} d\Xi = 0 \qquad \forall \quad (x_i, t) \quad , \tag{2.3}$$

where the Maxwell-Boltzmann equilibrium distribution g has a fixed form and can be derived from physical considerations (Cercigani[5]); we write it as

$$g(x_i, u_i, \xi, t) = A e^{-\lambda((u_i - U_i)^2 + \xi^2)}, \tag{2.4}$$

where the parameters A, U_i and λ are functions of x_i and t. After combining the conservation constraint of Eq.(2.3) with Eq.(2.2), and with the assumption of constant τ, we can find the relation between the equilibrium distribution function g and the macroscopic mass (ρ), momentum (P_i) and energy (ϵ) densities by insisting that

$$\begin{pmatrix} \rho \\ P_i \\ \epsilon \end{pmatrix} = \int \begin{pmatrix} 1 \\ u_i \\ \frac{1}{2}({u_i}^2 + \xi^2) \end{pmatrix} g d\Xi. \tag{2.5}$$

There are five parameters in g, and five macroscopic quantities — the preceding equations for the moments of g define a one-to-one correspondence between these two sets of variables:

$$\begin{pmatrix} \rho \\ P_i \\ \epsilon \end{pmatrix} = \begin{pmatrix} A\pi^{(K+3)/2}\lambda^{-(K+3)/2} \\ \rho U_i \\ \frac{1}{2}\rho({U_k}^2 + \frac{K+3}{2\lambda}) \end{pmatrix}. \tag{2.6}$$

For convenience in numerical calculations, we have used ρ, λ, U_i instead of A, λ, U_i to describe the Maxwellian distribution function (see Appendix B). By solving Eq.(2.6), all parameters in the Maxwellian g can be determined explicitly from ρ, P_i and ϵ to give

$$\begin{pmatrix} \rho \\ U_i \\ \lambda \end{pmatrix} = \begin{pmatrix} \rho \\ P_i/\rho \\ (K+2)\rho/(4(\epsilon - \frac{1}{2}\rho{U_k}^2)) \end{pmatrix}. \tag{2.7}$$

So, from the macroscopic quantities, we can uniquely give the equilibrium distribution function g, toward which the real gas distribution function f in the BGK model tends.

The formal integral solution for f in Eq.(2.1) is given as (see [28])

$$f(x_i, u_i, \xi, t) = \int_{t_0}^{t} e^{-[\eta(t)-\eta(t')]} g[x_i - u_i(t-t'), u_i, \xi, t'] \frac{dt'}{\tau[x_i - u_i(t-t'), t']} + e^{-\eta(t)} f_0(x_i - u_i t, u_i, \xi), \tag{2.8}$$

where

$$\eta(s) = \int_{t_0}^{s} \frac{ds'}{\tau[x_i - u_i(s-s'), s']} \tag{2.9},$$

a result which may be verified by substitution into the BGK equation. By introducing the above solution into the compatibility conditions (Eq.(2.3)), we find the following set of coupled nonlinear integral equations for the parameters of g:

$$\int \psi_\alpha e^{-\psi_\alpha \chi_\alpha(x_i,t)} d\Xi = \int \psi_\alpha \int_{t_0}^{t} e^{-\psi_\beta \chi_\beta(x_i{}',t') - \eta(x_i,t) + \eta(x_i{}',t')} \frac{dt'}{\tau(x_i{}',t')} d\Xi$$
$$+ e^{-\eta(x_i,t)} \int \psi_\alpha f_0(u_j, \xi, x_i{}'') d\Xi \qquad (2.10)$$

where $x_i{}' = x_i - u_i(t-t')$ in the first integral, $x_i{}'' = x_i - ut$ in the second,

$$\psi_\alpha = \{1, u_1, u_2, u_3, \frac{1}{2}(u_k{}^2 + \xi^2)\},$$

and

$$\chi_\alpha = (-ln(A), -2\lambda U_1, -2\lambda U_2, -2\lambda U_3, 2\lambda). \qquad (2.11)$$

Eqs.(2.10), when supplemented with appropriate boundary conditions, are valid all the way from the Euler regime (in the limit $\tau = 0$), through the Navier-Stokes regime (small, non-zero τ) to free molecular flow at $\tau = \infty$. (A derivation of the Euler and Navier-Stokes equations from the above integral equation is given in Appendix A.).

As we can see from Appendix A, the collision time τ in Eq.(2.1) plays a crucial role in the connection between the BGK model and the Navier-Stokes equations. From simple gas-kinetic theory the physical collision time is given by $\tau = l/\bar{v}$, where l is the mean free path, which can be written as a function of local number density n and the collision cross section σ, ($l \propto 1/(n\sigma)$); the mean molecular velocity $\bar{v}$ is proportional to the square-root of the gas temperature. Putting these together we find that the collision time is given by

$$\tau = C_1 \frac{\sqrt{\lambda}}{\rho}, \qquad (2.12)$$

where both the temperature term λ ($\lambda = 1/k\bar{T}$, where k is the Boltzmann constant and $\bar{T}$ is temperature) and the density ρ are a functions of x_i, t. All proportionality constants are included in the parameter C_1 in Eq.(2.12). For a particular example let's consider the Maxwell molecule, for which the potential Ψ between two molecules is $\Psi = \hat{K}/r^4$, where $\hat{K}$ is a constant and r is the distance. The collision time for this case is

$$\tau = \frac{5\sqrt{\pi}K_n}{8\rho}, \tag{2.13}$$

where K_n is the Knudsen number, and is proportional to the free stream mean free path ℓ_∞ , given by

$$\ell_\infty = \frac{16\mu_\infty}{5\rho_\infty\sqrt{2\pi RT_\infty}}. \tag{2.14}$$

In Eq.(2.14), μ is the viscosity coefficient and R is the gas constant (Kogan [19]).

Specifically, for the BGK model (see Appendix A), the relation between the collision time and the dynamical viscosity is

$$\eta = \tau p, \tag{2.15}$$

where p is the gas pressure. The kinematic viscosity ν is defined as $\nu = \eta/\rho$. Usually in fluid problems, the Reynolds number Re is given as $Re = UL/\nu$, where U and L are characteristic velocity and length scales. From the above equations, we can get the unknown parameter C_1 (*cf. Eq.(2.12)*) in terms of other known quantities for the numerical Navier-Stokes simulation. We find that

$$C_1 = \left(\frac{UL}{Re}\right)\left(\frac{\rho^2}{\sqrt{\lambda}p}\right), \tag{2.16}$$

where the velocity U can also be expressed as a function of the Mach number M and sound speed c as $U = Mc$.

To this point, we have given an introduction of the kinetic BGK model and its relation to the Navier-Stokes equations. Theoretically, if we can precisely solve the BGK model (Eq.(2.8)), the hydrodynamic Navier-Stokes equations are solved automatically. Beginning in the next section, we will present one of the new numerical approachs to the BGK model, and demonstrate its advantages for numerical hydrodynamics.

2.3 Numerical Approximations of the BGK Model

In upwind numerical schemes, the most generally used method is to evaluate the numerical fluxes through the cell boundary, and the accuracy of the scheme depends mainly on the accuracy of the fluxes. In order to get the fluxes, two computational stages have to be implemented. The first is the reconstruction stage, in which all physical quantities get interpolated to prepare initial data, and the second is the evolution stage, in which the gas flow evolves from the initial interpolated data according to the approximate governing equation in each time step. The governing equations for the gas flow can be Euler, Navier-Stokes, Boltzmann or any other kind of equations , which are correct in certain physical situations. Specifically, in this section, we illustrate the initial condition we use in our gas-kinetic hydrodynamic scheme, and mainly emphasize the numerical method of approximating the time-dependent BGK model — the governing dynamic equation for our gas simulation. The detailed interpolation scheme to get the required initial condition for the mass, momentum and energy will be left to the numerical results section. Also, in order to simplify our notation for explaining the scheme, in the following we give a numerical scheme in two dimensions. One and three dimensional schemes can be found by using similar strategies. It is true that the leap from two to three dimensions in our gas kinetic scheme is not as large as in other schemes starting from the Euler or Navier-Stokes equations directly.

As was explained in chapter 1, to get numerical fluxes, we first need to know the gas distribution function. The main problem in setting up a numerical BGK scheme is the calculation of the real gas distribution function f at a certain point in a two-dimensional space (x, y); then we integrate certain moments of f to get the numerical fluxes at this point. Considering a point $(x = 0, y = 0)$ in the two dimensional space, and assume that at this point, at the beginning of each time step (which is assumed to be $t = 0$) , the local equilibrium Maxwellian distribution function g is

$$g(x = 0, y = 0, t = 0) = Ae^{-\lambda((u-U)^2+(v-V)^2+\xi^2)}, \tag{2.17}$$

where A, λ, U and V are local constants. The Taylor expansion of the Maxwellian distribution in the neighborhood of this point (to the first order in space and time) can be written as

$$g(x, y, t) = g(0, 0, 0)(1 + ax + by + \hat{A}t), \tag{2.18}$$

where the velocity dependences of the coefficients a, b and $\hat{A}$ are given by

$$a = a_1 + a_2 u + a_3 v + a_4(u^2 + v^2 + \xi^2),$$

$$b = b_1 + b_2 u + b_3 v + b_4(u^2 + v^2 + \xi^2),$$

and

$$\hat{A} = \hat{A}_1 + \hat{A}_2 u + \hat{A}_3 v + \hat{A}_4(u^2 + v^2 + \xi^2). \tag{2.19}$$

All coefficients $a_1, a_2, ..., \hat{A}_4$ can also be regarded as locally constant, and the u, v, ξ dependences come from the Taylor expansion of the Maxwellian distribution.

For any numerical scheme, the initial discrete macroscopic mass $\rho(x, y, 0)$, momentum $P_i(x, y, 0)$ and energy $\epsilon(x, y, 0)$ densities (or equivalent information) at $t = 0$ must be given. We can also use the Taylor expansion to expand the macroscopic quantities around the point $(x = 0,\ y = 0)$ as

$$\rho(x, y, 0) = \rho(0, 0, 0)(1 + \rho_1 x + \rho_2 y)$$

$$P_x(x,y,0) = P_x(0,0,0)(1 + P_{x1}x + P_{x2}y)$$

$$P_y(x,y,0) = P_y(0,0,0)(1 + P_{y_1}x + P_{y_2}y)$$

and

$$\epsilon(x,y,0) = \epsilon(0,0,0)(1 + \epsilon_1 x + \epsilon_2 y), \tag{2.20}$$

where $\rho(0,0,0), \rho_1, ..., \epsilon_2$ are local constants also. The interpolation for all of these macroscopic quantities can be obtained by using the well-known TVD or ENO techniques, and the expansion point could be located on the cell boundary or inside a cell for a real problem. From Eq.(2.20), one can appreciate the multidimensionality in the above expansions, where both x and y dependences are included in the interpolation. Also, as we can see in the following, in our numerical scheme all information in Eq.(2.20) will be used to follow the gas evolution according to the BGK model with some reasonable approximation, and the final numerical fluxes at the point $(x = 0, y = 0)$ are uniquely determined by the expansion constants.

By putting Eq.(2.20) and Eq.(2.18) into Eq.(2.5), the mass, momentum and energy density expansions at time $t = 0$ give a unique solution for the corresponding equilibrium state $g(0,0,0)$ and its expansion parameters a and b in Eq.(2.19). The four parameters in the Maxwellian distribution $g(0,0,0)$ can be found from the 2-D version of Eq.(2.6), where ρ, P_x, P_y and ϵ are replaced by the interpolated quantities $\rho(0,0,0), P_x(0,0,0), P_y(0,0,0)$ and $\epsilon(0,0,0)$ of Eq.(2.20). After getting $g(0,0,0)$, the x-dependent a term in Eq.(2.19) can also be obtained by equating the x-dependent moments of g to the x-dependent terms in the mass, momentum and energy expansions. Thus we find

$$\begin{pmatrix} \rho_1/\rho(0,0,0) \\ P_{x1}/\rho(0,0,0) \\ P_{y_1}/\rho(0,0,0) \\ 2\epsilon_1/\rho(0,0,0) \end{pmatrix} = (\mathcal{A}) \begin{pmatrix} a_1 \\ a_2 \\ a_3 \\ a_4 \end{pmatrix}, \tag{2.21a}$$

where

$$(\mathcal{A}) = \begin{pmatrix} 1 & U & V & \mathcal{B}_1 \\ U & U^2 + 1/2\lambda & UV & \mathcal{B}_2 \\ V & UV & V^2 + 1/2\lambda & \mathcal{B}_3 \\ \mathcal{B}_1 & \mathcal{B}_2 & \mathcal{B}_3 & \mathcal{B}_4 \end{pmatrix}, \tag{2.21b}$$

$$\mathcal{B}_1 = U^2 + V^2 + (K+2)/2\lambda,$$

$$\mathcal{B}_2 = U^3 + V^2 U + (K+4)U/2\lambda,$$

$$\mathcal{B}_3 = V^3 + U^2 V + (K+4)V/2\lambda$$

and

$$\mathcal{B}_4 = (U^2 + V^2)^2 + (K+4)(U^2+V^2)/\lambda + (K^2 + 6K + 8)/4\lambda^2.$$

Fortunately, the above symmetric matrix (Eq.(2.21b)) can be inverted analytically,

$$(\mathcal{A}^{-1}) = \begin{pmatrix} (K+3) + (2\lambda + \hat{\mathcal{B}}_1)\hat{\mathcal{B}}_5 & -2U(\lambda + \hat{\mathcal{B}}_1) & -2V(\lambda + \hat{\mathcal{B}}_1) & \hat{\mathcal{B}}_1 \\ -2U(\lambda + \hat{\mathcal{B}}_1) & 2(\lambda - U\hat{\mathcal{B}}_2) & -2V\hat{\mathcal{B}}_2 & \hat{\mathcal{B}}_2 \\ -2V(\lambda + \hat{\mathcal{B}}_1) & -2V\hat{\mathcal{B}}_2 & 2(\lambda - V\hat{\mathcal{B}}_3) & \hat{\mathcal{B}}_3 \\ \hat{\mathcal{B}}_1 & \hat{\mathcal{B}}_2 & \hat{\mathcal{B}}_3 & \hat{\mathcal{B}}_4 \end{pmatrix}, \tag{2.21c}$$

$$\hat{\mathcal{B}}_1 = 4\lambda^2(U^2 + V^2 - (K+2)/2\lambda)/(2K+4),$$

$$\hat{\mathcal{B}}_2 = -8\lambda^2 U/(2K+4),$$

$$\hat{\mathcal{B}}_3 = -8\lambda^2 V/(2K+4),$$

$$\hat{\mathcal{B}}_4 = 4\lambda^2/(2K+4)$$

and

$$\hat{\mathcal{B}}_5 = U^2 + V^2 - (K+2)/2\lambda.$$

So, the analytic solutions for $a_1 \ldots a_4$ can be expressed in terms of $\rho_1/\rho(0,0,0)$, ..., $2\epsilon_1/\rho(0,0,0)$. For the b term in Eq.(2.19), similar equations can be solved by using $\rho_2/\rho(0,0,0)$, ... ,$2\epsilon_2/\rho(0,0,0)$ on the left side of Eq.(2.21a), while the parameters $a_1, \ldots, a_4$ are replaced by $b_1, \ldots, b_4$ on the right side. At this point, all the unknowns in a and b in the Taylor expansion of the Maxwellian distribution at $t = 0$ have been obtained from the initial mass, momentum and energy distributions.

The time derivative ($\hat{A}$) term in Eq.(2.18) contains the only unknown quantities in the expansion of g. In the following, we first use the general integral solution of the BGK model (Eq.(2.8)), and then determine $\hat{A}$ implicitly from the conservation constraints (cf. Eq.(2.3)). The general integral solution of the BGK model in two dimensions with the expansion of g (for locally constant τ) can be written as

$$f(x,y,t) = \frac{1}{\tau}\int_0^t g(0,0,0)(1+ax'+by'+\hat{A}t')e^{-(t-t')/\tau}dt' + e^{-t/\tau}f_0(x-ut,y-vt), \tag{2.22a}$$

where

$$x' = x - u(t-t'), y' = y - v(t-t'), \tag{2.22b}$$

are the trajectories for each particle (*i.e.*, the characteristics) and f_0 is the initial value of the true distribution function at $t=0$. The analysis for f_0 will be given in the next two subsections. The physical considerations which lead to different expressions for f_0 play a crucial role in our schemes.

By putting Eq.(2.18) into Eq.(2.22a), we find

$$\begin{aligned} f(x,y,t) = g(0,0,0)\big((1-e^{-t/\tau})(1+ax-\tau ua+by-\tau vb-\tau\hat{A}) + te^{-t/\tau}(ua+vb) \\ +t\hat{A}\big) + e^{-t/\tau}f_0(x-ut,y-vt). \end{aligned} \tag{2.23}$$

In order to get numerical fluxes across the cell boundary of the numerical mesh, the above equation needs to be integrated along the boundary element $d\vec{l} = \alpha_1 d\vec{x} + \alpha_2 d\vec{y}$. Although the integration for a small element can be easily implemented in the above equation, for simplicity, we assume that the cell boundary is located at $x=0$ and extends from $-1/2$ to $1/2$ in the $\hat{y}$-direction. The linear y-dependent term in the above equation disappears automatically when we integrate over dy to obtain fluxes. Therefore, at the end the following terms remain:

$$\begin{aligned} f(0,0,t) = g(0,0,0)\big((1-e^{-t/\tau})(1-\tau ua-\tau vb-\tau\hat{A}) + te^{-t/\tau}(ua+vb) + t\hat{A}\big) \\ + e^{-t/\tau}f_0(-ut,-vt), \end{aligned} \tag{2.24}$$

The unknown quantities in the preceding equation are the time expansion part $\hat{A}$ of Eq.(2.18) and the initial gas distribution function f_0. These two are closely related, and their evaluation distinguishes different schemes. Due to the fact that Eq.(2.24) is derived from a Taylor expansion of the Maxwellian (Eq.(2.18)), in the following, we introduce two kinds of schemes, the first one is called **METS** (Maxwellian Expansion Transport for Subsonic gas flow) scheme, which is correct for subsonic or slightly supersonic flow, and the second one is called **MET** (Maxwellian Expansion Transport) which works for both subsonic and supersonic flow.

2.3.1 METS Schemes

The **METS** scheme comes in two versions, which we call **METS-I** and **METS-II**. At the beginning of each time step $t = 0$, the real gas distribution function f_0 should depend on the physical situation in the flow. In a smooth region, f_0 can be regarded as being a local thermodynamical equilibrium state, or so-called LTE state, which has been widely used in many physical problems, such as the calculation of absorption and emission lines in radiative transfer. The meaning of LTE in the present context is that we may apply the equilibrium relations of statistical mechanics and thermodynamics at local values of the temperature and density for particles moving with the fluid. LTE should be correct in most physical situations away from extreme non-equilibrium states, such as shock fronts, and it provides a convenient method for computing the particle distribution functions. Under this assumption we can assume that f_0 is equal to the Maxwellian distribution g initially, which is to say

$$f_0(x,y,t=0) = g(x,y,t=0) = g(0,0,0)(1+ax+by), \qquad (2.25)$$

where all parameters in $g(x,y,0)$ are known. Putting the above condition into Eq.(2.24), we get

$$f(0,0,t)=g(0,0,0)\big(1+\tau(-1+e^{-t/\tau})(au+vb)+(t-\tau+\tau e^{-t/\tau})\hat{A}\big). \qquad (2.26)$$

At this time, the only unknown parameter for finding $f(0,0,t)$ in the above equation is $\hat{A}$, and the method of evaluating $\hat{A}$ distinguishes our schemes from all other Boltzmann-type schemes.

Before going on to determine the $\hat{A}$ term in Eq.(2.26), let's define some notation to simplify the mathematical representation. Let

$$<\ldots>=\int\begin{pmatrix}1\\ u\\ v\\ \frac{1}{2}(u^2+v^2+\xi^2)\end{pmatrix}(\ldots)d\Xi, \qquad (2.27)$$

be the four moments of some function defined on the phase space. The conservation constraint (Eq.(2.3)) in two dimensions (for locally constant τ) can be expressed simply as

$$<f-g>=0, \qquad (2.28)$$

for arbitrary x,y and t. (It is important to remember that Eq.(2.28) is actually 4 scalar equations.)

One way to get the $\hat{A}$ term in Eq.(2.26) is to use the condition Eq.(2.28), but we cannot use it everywhere in space and time. The limitation in the Taylor expansion of g restricts us to finding $\hat{A}$ by using the average of equation (2.28) at $x=0, y=0$ along the time axis from 0 to T, where T is the CFL time step. Because of the assumption $g(0,0,t)=g(0,0,0)(1+\hat{A}t)$ in Eq.(2.18), we find

$$f(0,0,t)-g(0,0,t)=g(0,0,0)(\tau(-1+e^{-t/\tau})(ua+vb+\hat{A})). \qquad (2.29)$$

Inserting the above equation into Eq.(2.28) and integrating over time, we get

$$<g(0,0,0)(ua+bv+\hat{A})>=0. \qquad (2.30a)$$

[Actually, in equation (2.29), $(ua+vb+\hat{A})$ have a common time-dependent factor; the above derived equation (Eq.(2.30a)) is correct for all times at $(x=0, y=0)$.] The four equations in Eq.(2.30a) uniquely give the four unknowns in $\hat{A}$ by solving a matrix similar to Eq.(2.21a), and the closed form solution is given by

$$A_\alpha = (\mathcal{A})^{-1}{}_{\alpha\beta} \frac{< -g(0,0,0)(ua+bv) >_\beta}{\rho(0,0,0)}, \qquad (2.30b)$$

where A_α is the unknown parameter in $\hat{A}$, $(\mathcal{A})^{-1}$ is the inverse matrix of $\mathcal{A}$ (Eq.(2.21c)) and $< ... >_\beta$ is the βth component of the four scalar moments in $< ... >$. Once this has been done, all parameters in the time-dependent distribution function $f(0,0,t)$ are known. The total fluxes densities at $(0,0)$, integrated over T, in the $\hat{x}$-direction are

$$\begin{pmatrix} F_\rho \\ F_{P_x} \\ F_{P_y} \\ F_\epsilon \end{pmatrix} = \int\int_0^T u \begin{pmatrix} 1 \\ u \\ v \\ \frac{1}{2}(u^2+v^2+\xi^2) \end{pmatrix} f(0,0,t)d\Xi dt. \qquad (2.31)$$

Using the notation of Eq.(2.27), we can rewrite the above equation as

$$F_\alpha = \beta_1 < ug(0,0,0) >_\alpha + \beta_2 < (u^2a+uvb)g(0,0,0) >_\alpha + \beta_3 < \hat{A}g(0,0,0) >_\alpha, \qquad (2.32a)$$

where

$$\beta_1 = \int_0^T dt = T,$$

$$\beta_2 = \int_0^T [\tau(-1+e^{-t/\tau})]dt = -\tau T + \tau^2(1-e^{-T/\tau}),$$

$$\beta_3 = \int_0^T [t+\tau(-1+e^{-t/\tau})]dt = \frac{1}{2}T^2 - \tau T + \tau^2(1-e^{-T/\tau}), \qquad (2.32b)$$

and the subscript on the angular brackets refer to the four components of Eq.(2.27). As we can see, the total mass, momentum and energy transport are not linear functions of the time step T; they depend on the time-dependent gas distribution function. In other words, there is a relaxation process in our scheme for the gas flow to approach the equilibrium state within each time step.

The main part of the numerical calculation in Eq.(2.32) is based on the evaluation of the moments of the Maxwellian. It looks very complicated, but owing to the simple recursion relations among different moments, the programming is not hard at all (see Appendix B). At this point, we have finished the exposition of the **METS-I** scheme, and numerical tests of this scheme will be presented in the next section. In the following, we will give a slight modification to the above scheme, which will be called the **METS-II** scheme.

For subsonic gas flow, and away from boundaries and discontinuities, the integral solution of the BGK model in Eq.(2.22a) can be simplified by using $-\infty$ as the lower limit of the integral, and as a consequence, the initial term of $f_0(x-ut)$ in Eq.(2.22a) disappears. The solution under this assumption is

$$f(x,y,t)=\frac{1}{\tau}\int_{-\infty}^{t} g(0,0,0)(1+ax'+by'+\hat{A}t')e^{-(t-t')/\tau}dt', \tag{2.33}$$

where $x'=x-u(t-t')$ and with the same Taylor expansion for $g(x,y,t)$ in Eq.(2.18). The above integration can be done explicitly to give

$$f(0,0,t)=g(0,0,0)(1-\tau ua-\tau vb+(t-\tau)\hat{A}). \tag{2.34}$$

Since $t=0$ is assigned as the initial time for each time step, putting $t=0$ in the above equation gives the initial gas distribution function $f_0(0,0,0)$,

$$f_0(0,0,0)=g(0,0,0)(1-\tau(ua+vb+\hat{A})), \tag{2.35}$$

which is different from the assumption of $f_0(0,0,0)=g(0,0,0)$ in **METS-I**. But, we can see in the following that their corresponding macroscopic quantities are the same.

In order to get the $\hat{A}$ term, we can use the same strategies as in the **METS-I** scheme. From $g(0,0,t)=g(0,0,0)(1+\hat{A}t)$ in Eq.(2.18), we obtain

$$f(0,0,t)-g(0,0,t)=g(0,0,0)(-\tau)(ua+vb+\hat{A}). \tag{2.36}$$

Inserting the above equation into the conservation constraints (Eq.(2.28)), and integrating over time (not necessary here) gives the same formula as Eq.(2.30) for determining the $\hat{A}$ term, namely

$$< g(0,0,0)(ua + bv + \hat{A}) >= 0. \tag{2.37}$$

If we take the moments $< ... >$ of Eq.(2.35), and use Eq.(2.37), we find that the moments $< f(0,0,0) >=< g(0,0,0) >$, which means that the corresponding macroscopic quantities for f and g are the same at $x = 0, y = 0$ and $t = 0$. After getting the $\hat{A}$ term in Eq.(2.37) as we did in **METS-I** schemes, the final numerical flux transport for the **METS-II** scheme is

$$F_\alpha = \beta_1 < ug(0,0,0) >_\alpha + \beta_2 < (u^2 a + uvb)g(0,0,0) >_\alpha + \beta_3 < \hat{A}g(0,0,0) >_\alpha, \tag{2.38a}$$

where

$$\beta_1 = \int_0^T dt = T,$$

$$\beta_2 = \int_0^T [-\tau] dt = -\tau T,$$

and

$$\beta_3 = \int_0^T [t - \tau] dt = \frac{1}{2}T^2 - \tau T. \tag{2.38b}$$

Comparing Eq.(2.32) with Eq.(2.38), we can see that, to the first order of τ, the **METS-I** and **II** schemes are identical. The terms of first order in τ correspond to the Navier-Stokes equations (see Appendix A). In the numerical part (section 2.4), we will find that the two versions of **METS** give almost identical simulation results. More specifically, the relative flux transport differences for these two schemes are one order higher than the Navier-Stokes fluxes, *i.e.*

$$\frac{\Delta F_\rho}{F_\rho} \simeq (\frac{\tau}{T})^2,$$

$$\frac{\Delta F_P}{F_P} \simeq (\frac{\tau}{T})^2$$

and

$$\frac{\Delta F_\epsilon}{F_\epsilon} \simeq (\frac{\tau}{T})^2, \tag{2.39}$$

where τ is usually one order of magnitude smaller than the time step T for hydrodynamic simulations.

METS-I and **METS-II** schemes are second order accurate schemes in both space and time from the consideration of the initial Taylor expansions. To capture higher order effects (higher than the Navier-Stokes equations), higher order numerical BGK schemes are necessary, but probably not sufficient. The extension to third order is straightforward in these cases, and can be found by expanding g to second order in x, y and t,

$$g(x,y,t) = g(0,0,0)(1 + ax + cx^2 + by + dy^2 + exy + \hat{A}t + \hat{B}t^2 + \hat{C}xt + \hat{D}yt), \tag{2.40a}$$

where the terms of $g(0,0,0), a, b, c, d$ and e can be found using the initial mass, momentum and energy interpolations, and the terms $\hat{A}$ through $\hat{D}$ can be obtained from the following conditions at $(x = 0, y = 0)$:

$$\int_0^T < f - g > dt = 0,$$

$$\frac{\partial}{\partial x} \int_0^T < f - g > dt = 0,$$

$$\frac{\partial}{\partial y} \int_0^T < f - g > dt = 0,$$

and

$$\frac{\partial}{\partial t} \int_0^T < f - g > dt = 0. \tag{2.40b}$$

When $\hat{A}, \hat{B}, \hat{C}$ and $\hat{D}$ have be found from these equations, f can be obtained from Eq.(2.22) using Eq.(2.40a) as the equilibrium g term. The third order numerical

METS-I code has been found and used on some one-dimensional test cases, but the improvement in the numerical results is slight in the discontinuity regions of gas flows. This procedure can be continued to arbitrarily high order for the numerical BGK scheme. Since this scheme is solely based on the local properties of the gas distribution function, it distinguishes it from spectral methods, where the global Fourier expansion has to be taken into account; obviously a very high-order (*e.g.* 20th order) scheme needs to include more and more cells in the interpolation for g.

In this section, we have developed two numerical schemes for solving the BGK model, called **METS-I** and **METS-II**. The differences between them are: the first one assumes that f_0 at time $t = 0$ is Maxwellian and the second one doesn't give the Maxwellian distribution itself, but the corresponding macroscopic quantities (ρ, P_i and ϵ) are same. For the final numerical fluxes, these differences are of order τ^2, which is beyond the Navier-Stokes validity region. These differences have almost no effect on simulation results, especially in the regions away from discontinuities and boundaries, because Local Thermodynamic Equilibrium is a very good approximation in such regions. In the extreme regions, as in the neighborhood of a discontinuity, both schemes are inadequate to describe the flow, since the local f_0 should not be Maxwellian in **METS-I** scheme, and the integration from $-\infty$ will definitely cut across the discontinuity, which invalidates the condition for the Taylor expansion for g in **METS-II** scheme.

Another easily confused question is this: LTE assumes the local Maxwellian distribution, which corresponds to the Euler equation, since the viscosity and heat conductivity terms disappear when one takes moments of the Maxwellian. Then how could one simulate the Navier-Stokes equations as claimed under this assumption? To answer this question, first we need to know that the real viscosity takes effect in the dynamical evolution stage. The main part of our scheme is to evaluate the time-dependent distribution function f at a cell boundary, which takes into account dynamical physical process for describing the flow from the initial local Maxwellian, and the final distribution f itself is not generally a Maxwellian, but a combination of several functions (*cf.* Eq.(2.32a) and Eq.(2.38a)); the weights for the different "pieces" in f are determined by the BGK model. The numerical fluxes calculated from f will give the Navier-Stokes solutions in a natural way. In other words, physical laws govern the dynamic description of the motion, and they are not related to the details of the initial gas distribution at all. Specifically, there is only one Navier-Stokes equation, but there could be an infinite number of initial distribution functions for the gas. So, the assumption $f = g$ as initial data at the beginning of each time step doesn't prevent one from following the time evolution of f; and this f is determined by the solutions of Navier-Stokes equations. Mathematically, the time step $T >> \tau$ for hydrodynamics makes the effects of the initial Maxwellian decay as $e^{-T/\tau}$, which means that the gas flow forgets its initial data quickly in the hydrodynamical regime in the process of approaching the equilibrium state. In numerical work, other sources of error, such as the truncation of the Taylor expansion in our case, are much more important than the assumption of that $f = g$ in the hydrodynamic limit, especially in regions where the discontinuities forbid using the smooth Taylor expansion. For rarefied gas flow, the assumption of $f = g$ naturally fails, and collisions will not change f so much that it "forgets" its higher moments in one time step.

2.3.2 MET Scheme

In the preceding section, we used the integral solution of the BGK model and the smooth expansion for g and f_0 around the point $(x = 0, y = 0, t = 0)$ to find the gas distribution function f during a time step at the cell boundary. The final expressions for the fluxes are uniquely determined by the initial Taylor expansions. This technique requires the gas flow to depend smoothly on position and time, and this means that there are no unresolved discontinuities with characteristic thickness much less than the size of one cell. In reality, for nonlinear flows, especially in the supersonic region, discontinuities are ubiquitous. In these "discontinuities", the particle distribution function changes dramatically, and this invalidates simple Taylor expansions. Our experiences shows that a pure **METS** code gives oscillatory results near discontinuities of the flow, even for the simple Sod test case, as shown in Fig.(3.2a). In this section we introduce a modification of the **METS** scheme to deal with regions treated as discontinuities in solutions of the Euler equations. This generalized code is called the **MET** scheme (Maxwellian Expansion Transport). We will show that it gives surprisingly good results both for subsonic and supersonic flow, and that nothing prevents this scheme from giving correct Navier-Stokes solutions as well.

One of the important questions is what the real distribution function $f_0(x, y, 0)$ should be in the neighborhood of the point $(x = 0, y = 0)$ at $t = 0$. In a smooth region, as we have seen in the last sub-section, LTE is a good physical assumption. However, if there is a discontinuity at or near $(x = 0, y = 0)$, f_0 can be a drastically varying function, and the assumption of $f = g$ fails automatically. For numerical purposes, in most cases, the cell size is much larger than the thickness of the physical discontinuity. The safest way to proceed here is, first, to interpolate f_0 separately on the both sides of the cell boundary. In a smooth region, the separate interpolations can be smoothly connected. At the same time, in the discontinuity regions , such as at a shock front, this assumption gives different interpolated values at the upstream and downstream regions and this "jump" is consistent with physical reality at the shock front. This is also similar to the Mott-Smith [24] model for the calculation of shock structure from the BGK model, where f is assumed to be a superposition of two different Maxwellians.

Since the BGK model assumes that the real gas distribution function will approach the equilibrium state through collisions, it is reasonable to expect the equilibrium state g to be smoother than f, and we can keep the same method as in Eq.(2.18) to expand it as

$$g(x,y,t) = g(0,0,0)(1 + ax + by + \hat{A}t). \tag{2.41}$$

For the initial real gas distribution function f_0, we interpolate it separately in the regions of $x < 0$ and $x > 0$; the resulting distribution function becomes

$$f_0(x,y,0) = \begin{cases} g^l(0,0,0)(1 + a^l x + b^l y), & x < 0 \\ g^r(0,0,0)(1 + a^r x + b^r y), & x > 0 \end{cases} \tag{2.42}$$

where g^l and g^r are local Maxwellians, and a^l, b^l, a^r and b^r have velocity dependences of the same sort as a and b in Eq.(2.19).

Similarly, the initial discrete mass, momentum and energy densities can be expanded as

$$\rho^l(x,y,0) = \rho^l(0,0,0)(1 + \rho^l{}_1 x + \rho^l{}_2 y)$$

$$P^l{}_x(x,y,0) = P^l{}_x(0,0,0)(1 + P^l{}_{x_1} x + P^l{}_{x_2} y)$$

$$P^l{}_y(x,y,0) = P^l{}_y(0,0,0)(1 + P^l{}_{y_1} x + P^l{}_{y_2} y)$$

and

$$\epsilon^l(x,y,0) = \epsilon^l(0,0,0)(1 + \epsilon^l{}_1 x + \epsilon^l{}_2 y), \tag{2.43}$$

for $x < 0$, with similar expansions for $\rho^r(x,y,0) ... \epsilon^r(x,y,0)$ for $x > 0$, where all parameters from $\rho^l(0,0,0)$ to $\epsilon_2{}^r$ are local constants. In a smooth region the macroscopic interpolations from the left and right sides are automatically close to each other; near a discontinuity they can have very different values. All parameters in $f_0(x,y,0)$ can be found in the same way as the quantities $g(0,0,0)$ and the a and b

terms in $g(x,y,0)$ from the interpolated macroscopic quantities. Following the new rule for the interpolation of f_0, the real gas distribution function $f(0,0,t)$ becomes

$$\begin{aligned} f(0,0,t) = {} & g(0,0,0)((1-e^{-t/\tau})(1-\tau ua-\tau vb-\tau \hat{A})+te^{-t/\tau}(ua+vb)+t\hat{A}) \\ & + e^{-t/\tau} f_0(-ut,-vt), \end{aligned} \tag{2.44}$$

with

$$f_0(-ut,-vt) = \begin{cases} g^l(0,0,0)(1-a^l ut-b^l vt), & u>0 \\ g^r(0,0,0)(1-a^r ut-b^r vt), & u<0. \end{cases} \tag{2.45}$$

The unknown parameter $\hat{A}$ in the distribution function $f(0,0,t)$ can be obtained by using the same conservation constraints at $(x=0, y=0)$ averaged over the whole time step T and $\int_0^T < g-f > dt = 0$, namely

$$\int \int_0^T \begin{pmatrix} 1 \\ u \\ v \\ \frac{1}{2}(u^2+v^2+\xi^2) \end{pmatrix} (g(0,0,t)-f(0,0,t)) d\Xi dt = 0, \tag{2.46a}$$

which gives

$$\begin{aligned} \beta_1 < \hat{A} g(0,0,0) > = {} & \beta_2 < g(0,0,0) > + \beta_3 < (ua+vb) g(0,0,0) > \\ & + \beta_4 (< g^l(0,0,0) >_{u>0} + < g^r(0,0,0) >_{u<0}) \\ & + \beta_5 (< (ua^l+vb^l) g^l(0,0,0) >_{u>0} \\ & + < (ua^r+vb^r) g^r(0,0,0) >_{u<0}), \end{aligned} \tag{2.46b}$$

where $< ... >_{u>0}$ is the integration $< ... >$in the space $u > 0$, $< ... >_{u<0}$ is the integration in the space $u < 0$, and all quantities on the right hand side of the above equation can be easily obtained by using Appendix B. Also,

$$\beta_1 = \tau T - \tau^2 (1-e^{-T/\tau}),$$

$$\beta_2 = -\tau (1-e^{-T/\tau}),$$

$$\beta_3 = -\tau T + 2\tau^2(1 - e^{-T/\tau}) - \tau T e^{-T/\tau},$$

$$\beta_4 = \tau(1 - e^{-T/\tau}),$$

and

$$\beta_5 = \tau T e^{-T/\tau} - \tau^2(1 - e^{-T/\tau}).$$

Eq.(2.46b) can be easily solved to get the moments $< \hat{A}g(0,0,0) >$, from which all unknowns of $\hat{A}$, namely A_1, A_2, A_3 and A_4 can be obtained as

$$A_\alpha = (\mathcal{A})^{-1}{}_{\alpha\beta} < \hat{A}g(0,0,0) >_\beta . \qquad (2.46c)$$

The main difference between **MET** and **METS** schemes is that it is necesary to evaluate error functions for the terms $< ... >_{u>0}$ and $< ... >_{u<0}$, but it is as fast to evaluate the error function as it is to compute a square root on modern computers.

At this point, for the new **MET** scheme, we can get the explicit function $f(0,0,t)$. In the same way, we can easily evaluate the mass, momentum and energy densities fluxes across the boundary for the whole time step T; these are

$$\begin{pmatrix} F_\rho \\ F_{P_x} \\ F_{P_y} \\ F_\epsilon \end{pmatrix} = \int\int_0^T u \begin{pmatrix} 1 \\ u \\ v \\ \frac{1}{2}(u^2 + v^2 + \xi^2) \end{pmatrix} f(0,0,t) d\Xi dt. \qquad (2.47a)$$

Specifically,

$$\begin{aligned} F_\alpha = {} & \beta_1' < ug(0,0,0) >_\alpha + \beta_2' < (u^2 a + uvb) g(0,0,0) >_\alpha \\ & + \beta_3' < (u\hat{A}g(0,0,0) >_\alpha + \beta_4' (< ug^l(0,0,0) >_{u>0,\alpha} + < ug^r(0,0,0) >_{u<0,\alpha}) \\ & + \beta_5' (< (u^2 a^l + uvb^l) g^l(0,0,0) >_{u>0,\alpha} + < (u^2 a^r + uvb^r) g^r(0,0,0) >_{u<0,\alpha}), \end{aligned} \qquad (2.47b)$$

where

$$\beta_1' = T - \tau(1 - e^{-T/\tau}),$$

$$\beta_2' = -\tau T + 2\tau^2(1 - e^{-T/\tau}) - \tau T e^{-T/\tau},$$

$$\beta_3' = \frac{T^2}{2} - \tau T + \tau^2(1 - e^{-T/\tau}),$$

$$\beta_4' = \tau(1 - e^{-T/\tau}),$$

and

$$\beta_5' = \tau T e^{-T/\tau} - \tau^2(1 - e^{-T/\tau}).$$

In the above **MET** scheme, we have tried to be more physically realistic by constructing an initially discontinuous distribution f_0. But this discontinuity is not intrinsically necessary in our scheme. For smooth flow, we don't need a discontinuity at all, as in the **METS** schemes. For Godunov-type schemes, the analysis is mainly based on the evaluation of discontinuous solutions which are required by the so-called Riemann solvers, and may not be present in the real gas flow. On the contrary, the integral solution of the BGK model can actually use any kind of initial distributions (to any order in space), continuous or discontinuous, across the cell boundary for both g and f. This kind of property will probably make it applicable to more physical situations than the Godunov-type schemes. Also, from Eq.(2.47), we can see that the **MET** scheme gives sub-timestep resolution, which is similar to the generalized Riemann problem.

2.4 Numerical Results

2.4.1 Non-Linear Initial Interpolations

In the last section, we passed over the question of interpolating the initial mass, momentum and energy distributions. Recently developed TVD and ENO methods provide excellent interpolation rules to prevent over-shooting in the interpolated quantities, especially in the discontinuity region. In our gas-kinetic schemes, the initial linearly distributed mass, momentum and energy are all used (including the slopes) to evaluate the final numerical fluxes from the integral BGK solution, so that the dependence of the final result on the initial interpolation should not be as sensitive as it is in Godunov-type schemes, where two constant states are used to get the fluxes. In the following, we give a rough ' non-linear ' limiter for our scheme, where the restriction on the interpolation is based solely on simple physical considerations. Since the same rules are imposed on the mass, momentum and energy, for simplicity, we just present the mass distribution evaluation.

As shown in Fig(3.1), let's first get the interpolation quantities in the $\hat{x}$ direction. We choose $x = 0$ at a cell wall, where the numerical fluxes are to be evaluated, and number the cells in the $\hat{x}$ direction $(1), (2), (3)$ and (4) with the boundary between cells (2) and (3) at $x = 0$. Let $\rho(i)$ be the discrete initial mass in each cell (i) at time $t = 0$. We first use these data to find $\rho(0,0,0)$ and ρ_1 in Eq.(2.20). We expand the density ρ around $x = 0$ as a cubic function

$$\rho(x,0,0) = \rho(0,0,0)(1 + \rho_1 x + \rho_2 x^2 + \rho_3 x^3), \tag{2.48}$$

where $\rho(0,0,0), \rho_1, \rho_2$ and ρ_3 are local constants. These coefficients are determined from the "conservative" condition

$$\rho(i) = \int_{x_{i-1/2}}^{x_{i+1/2}} \rho(x,0,0)dx \qquad , \qquad i = 1,2,3,4 \tag{2.49}$$

where $x_{i-1/2}$ and $x_{i+1/2}$ are the left and right boundaries of the cell i. There are four equations for the four unknowns in Eq.(2.48), and it is readily found that

$$\rho(0,0,0) = \frac{7}{12}(\rho(2) + \rho(3)) - \frac{1}{12}(\rho(1) + \rho(4)) \tag{2.50}$$

and

$$\rho_1 = \frac{\frac{5}{4}(\rho(3) - \rho(2)) - \frac{1}{12}(\rho(4) - \rho(1))}{\rho(0,0,0)} \quad . \tag{2.51}$$

Since we just need the linear term in x in our scheme, the interpolated values of ρ_2 and ρ_3 can be ignored.

In addition to the above interpolations, however, we require that the interpolated values $\rho(0,0,0)$ satisfy some reasonable constraints:

1). If $\rho(0,0,0)$ falls outside the range of the discrete values $[\rho(2),\rho(3)]$, we replace $\rho(0,0,0)$ with the value of $\rho(2)$ or $\rho(3)$ lying nearest to the previously computed $\rho(0,0,0)$.

2). If ρ_1 and $(\rho(3)-\rho(2))$ have opposite signs, we replace the values of $\rho(0,0,0)$ and ρ_1 with $\frac{1}{2}(\rho(2)+\rho(3))$ and $(\rho(3)-\rho(2))/\rho(0,0,0)$ respectively. This is exactly the same as second order central-difference interpolation.

For the **MET** scheme, we also need to determine the parameters of $\rho^l(0,0,0)$ and $\rho^r(0,0,0)$ for the left and right initial expansions in Eq.(2.43). For these quantities, we proceed in much the same way as above, but use quadratic interpolation on cells $(1),(2)$ and (3) for the left side quantities, and $(2),(3)$ and (4) for the right side. The determination of the first derivative terms ${\rho^l}_1$ and ${\rho^r}_1$ are rather different from that of ρ_1 in Eq.(2.51), because we insist on conservation of mass in cells (2) and (3), so we use

$$ {\rho^l}_1 = \frac{\rho^l(0,0,0)-\rho(2)}{2\rho^l(0,0,0)}, \tag{2.52a} $$

and

$$ {\rho^r}_1 = \frac{\rho(3)-\rho^r(0,0,0)}{2\rho^r(0,0,0)}. \tag{2.52b} $$

We sometimes need to use a lower order interpolation scheme than the quadratic one, if

$$ (\rho(2)-\rho(1))(\rho(4)-\rho(3)) \le 0. \tag{2.53} $$

When this happens, we find $\rho^l(0,0,0)$ from linear interpolation using cells (1) and (2), and follow a similar rule for the right side $\rho^r(0,0,0)$ from cells (3) and (4), where for ${\rho^l}_1$ and ${\rho^r}_1$ the same equations (Eq.(2.52)) are used.

The interpolation of the y-dependent variables in Eq.(2.20) and Eq.(2.43) can be found easily by using a central difference scheme, for example,

$$\rho_2 = \frac{((\rho(7)+\rho(8)) - (\rho(5)+\rho(6)))}{4\rho(0,0,0)},$$

$$\rho^l{}_2 = \frac{((\rho(7)) - \rho(5))}{2\rho^l(0,0,0)}$$

and

$$\rho^r{}_2 = \frac{(\rho(8) - \rho(6))}{2\rho^r(0,0,0)}. \tag{2.54}$$

But for a truely multidimensional scheme, some restrictions on the interpolations of the y-dependent variables would be necessary.

The concept of a nonlinear limiter was first used in CFD by van Leer [16], and the above interpolation rule is similar to using a non-linear limiter, but it does not exactly satisfy the TVD condition; for example, we don't insist on $[\rho(3) - \rho(2)][\rho^r(0,0,0) - \rho^l(0,0,0)] > 0$. We believe that interpolation is just one step in any numerical scheme; it doesn't uniquely determine the accuracy of the scheme, and any physically reasonable method should give a good result. On the other hand, if the gas evolution stage is physically correct, it should relax the interpolated values to the correct ones, as the particle collisions in the **MET** scheme do, to smear the unphysical initial " discontinuity " quickly. The important thing is that the overall slope should be correct, such as $\rho_1(\rho(3) - \rho(2)) > 0$. As recommended by A. Harten and C. Shu, we have tried to use some high-order ENO interpolations to get the expansion coefficients for f_0. Since just the linear terms are kept in the current scheme, the ENO interpolation doesn't substantially improve the simulation results.

In our schemes we separate the reconstruction and evolution stages clearly, and we don't need to use a very elaborate interpolation to couple the reconstruction and evolution to get a good result. For some Godunov-type schemes, since two constant states are used for the Riemann solver, the evolution properties are sometimes included in the reconstruction stage, such as the PPM code where the time-step and sound speed are used in the preparation of the initial constant states.

2.4.2 Numerical Examples

We have now presented the **METS** and **MET** schemes, and the only unknown parameter in our codes for a real gas flow problem is the collision time τ. As presented at the end of section 2.2, we have given the explicit formula for it in the limit of the Navier-Stokes equations, namely

$$\tau = \mathcal{C}_1 \frac{\sqrt{\lambda}}{\rho(0,0,0)}, \tag{2.55}$$

and the parameter C_1 is determined by the Reynold number Re and Mach number M of the flow. In order to validate the applicability of this scheme for the Navier-Stokes equations, in the following we give three Navier-Stokes test cases, where in all simulations $\gamma = 1.4$ is used, and $\mathcal{C}_1$ is determined by matching the value of ν in each problem.

- **Isotropic Turbulence Test Case**

In [25], Passot and Pouquet simulated two-dimensional, compressible , isotropic flows in the turbulence regime using a Fourier spectral collocation method. They identified three basic regimes: shock-free, weak shocks, and strong shocks. Subsequently, Erlebacher *et al.* [12]tried to develop a theory of compressible turbulence that contained a more refined characterization of the different regimes of compressible turbulence and contained a useful parameterization of initial conditions that permitted precise predictions of the asymptotic turbulence state. The direct simulation is limited to quite low Reynolds numbers, particular in the shock regime. Gibbs oscillations arose whenever the shocks were too thin for the grid to resolve.

In the following test case, we perform a two-dimensional simulation of compressible isotropic “turbulence” using the **METS I** and **METS II** codes. In order to have a comparison with other schemes, the simulation results from an ENO code is also presented. The initial "random" data was generated by G. Erlebacher on a computational domain of 128×128. The boundary conditions are periodic in both directions, the density, momentum and total energy are about $1, 2$ and 2000 on the average, and the viscosity is taken to be constant to make $Re = 150$. The initial 30 density contours are presented in Fig.(2.2a) for this problem.

Here we present the simulation results from three numerical schemes. The first one is the High-Order ENO Scheme (Shu *et al* [38]). Essentially non-oscillatory (ENO) schemes, first introduced by Harten and Osher [15] and Harten *et al* [14] can achieve uniformly high-order accuracy for the solutions of the Euler equations with sharp, essentially non-oscillatory shock transitions. The Navier-Stokes scheme used here applies the ENO method [37] to the advective part, and the diffusive part is approximated by standard centered differences. At the same time, a TVD Runge-Kutta type method (Shu and Osher [36]) is used to get third-order accuracy in time. The simulation result for the density contours using the ENO scheme is shown in Fig.(2.2b) (which was calculated by C.W. Shu), where the output time is at 150 CFL time steps. The contours show that a lot of small weak shocks have emerged and as we shall see later, there is vorticity generation around the shocked regions, which was predictable from Crocco’s theorem.

For the same problem, we did the simulation using both the **METS-I** and **METS-II** schemes. According to the initial condition for this problem and Eq.(2.16), the only unknown parameter C_1 can be derived, which has the numerical value 0.08533. Here the collision time τ plays an important role. Fig.(2.2c) and Fig.(2.2d) are two density contours from the **METS-I** and **METS-II** codes respectively at the output time of 50 CFL time steps. When comparing with the results from the

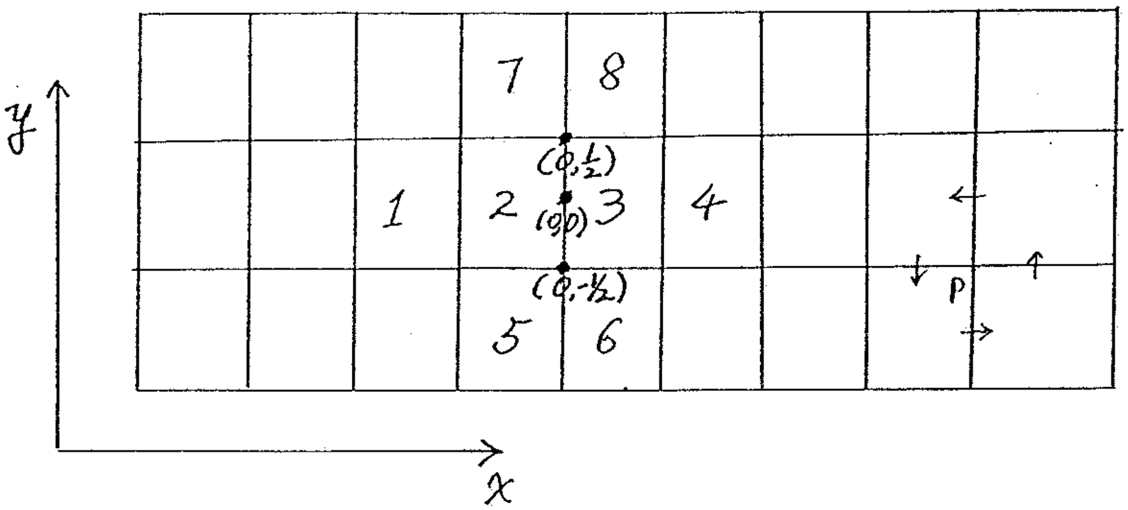

Figure 2.1 : The Computational Domain for Two-Dimension Calculations

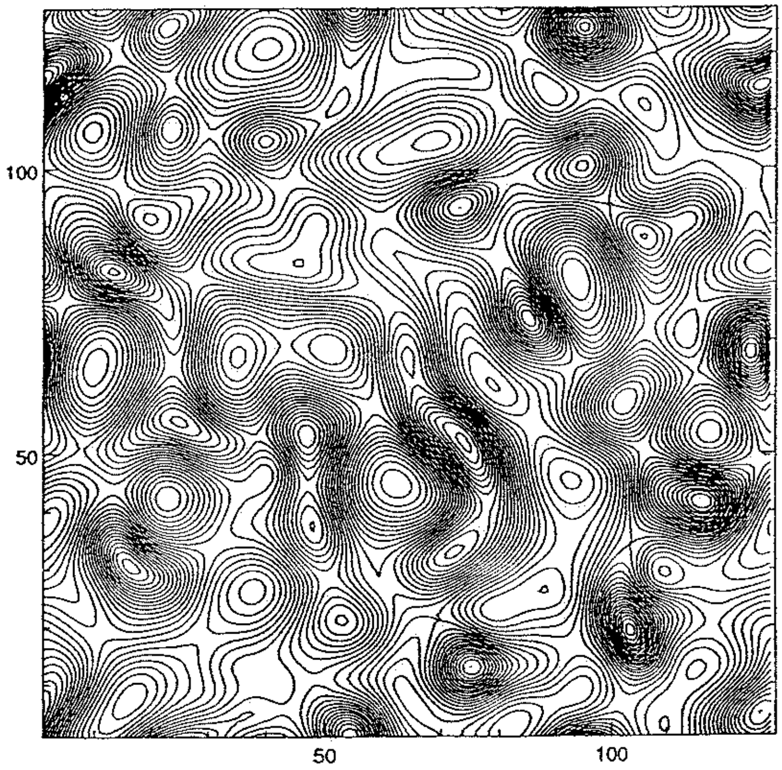

Figure 2.2a : The Initial Density Contours for the Isotropic Turbulence Flow

ENO scheme, we can easily find the similarities between them, and both of our gas kinetic schemes are comparable with the third-order Navier-Stokes ENO code. The time step for our code is about three times larger than that for the ENO scheme, and the reason for this will be given in point 3) in the conclusion part of this chapter. The slight differences between Fig.(2.2c) and (2.2d) are due to a slight difference in times at $N = 50$ for the two schemes.

In order to display the evolution of the disordered flow, we also show the vorticity contours at time step 50 in Fig.(2.2e). Due to the fact that vorticity depends on derivatives of the velocities the accurate evaluation of the derivative is crucial for this plot. We evaluate the velocity integral around a small area, then divide the integration by the area, as

$$\vec{\omega} = \frac{\oint \vec{v} \cdot d\vec{l}}{\oint d\vec{S}}, \tag{2.56}$$

where the path integral is along the cell around the point p shown in the Fig.(2.1). The average velocity at each boundary is evaluated from the same interpolation rule we used for the interpolation of density.

For a higher Reynolds number and for the same initial gas distribution, the physical viscosity should be reduced. The next test is to change the Reynolds number to 1,500 with the same initial condition (equivalently, to use $C_1 = 0.00853$ in our scheme), and the simulation results are shown in Fig.(2.4a) and Fig.(2.4b) for density and vorticity contours at our output time of 90 CFL time steps. From the figures, we can see that the structures become sharper than for the case of $Re = 150$, which are shown in Fig.(2.3a) and Fig.(2.3b) at the same number of time steps. Along with the decrease of physical viscosity, the artificial viscosity from the numerical approximation, arising from the linear interpolation of the macroscopic quantities, would definitely become dominant. So, at high Reynold number, we cannot say that all effects are real and physical (notice the noise in the vorticity

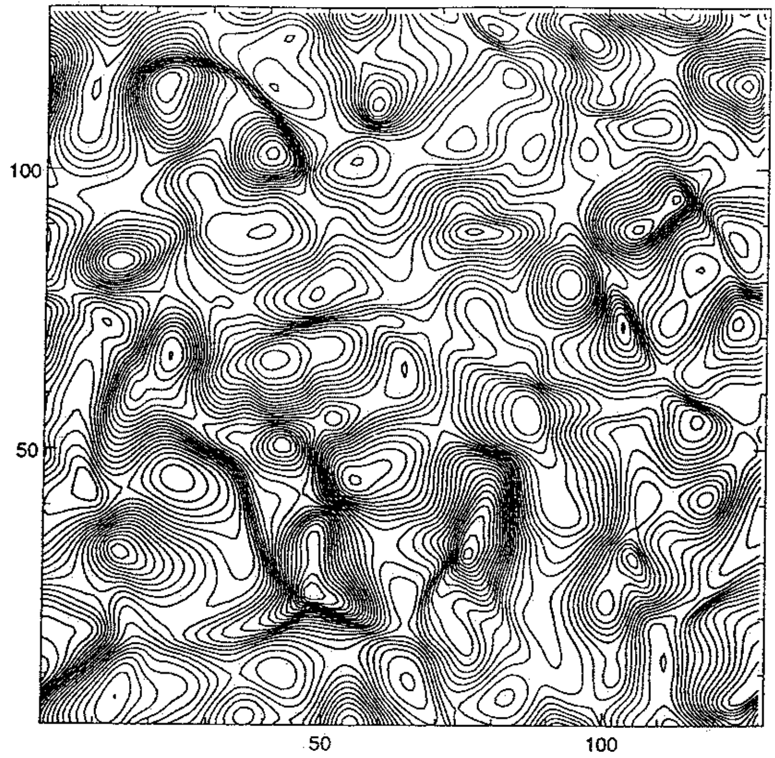

Figure 2.2b : Density Contours from **ENO** *Scheme at Time-Steps N=50*

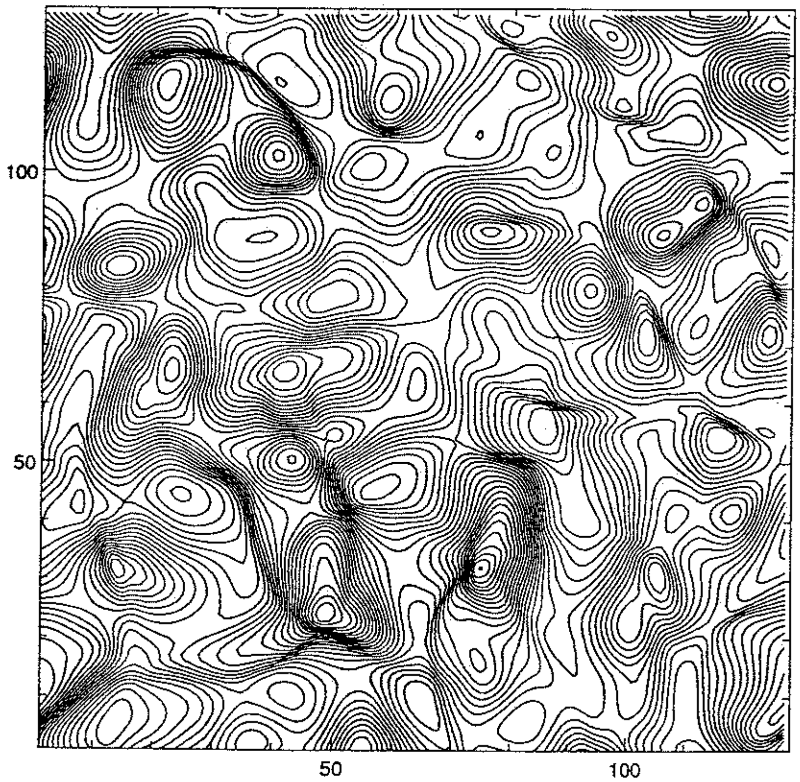

Figure 2.2c : Density Contours from **METS-I** *Scheme at Time-Step N=50*

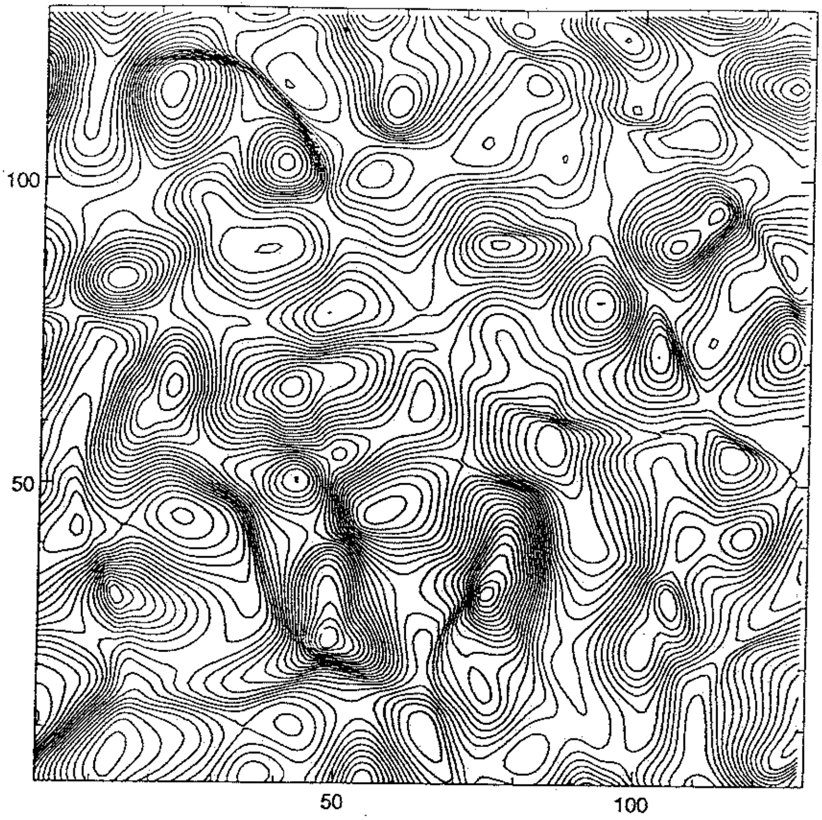

Figure 2.2d : Density Contours from **METS-II** *Scheme at Time-Steps N=50*

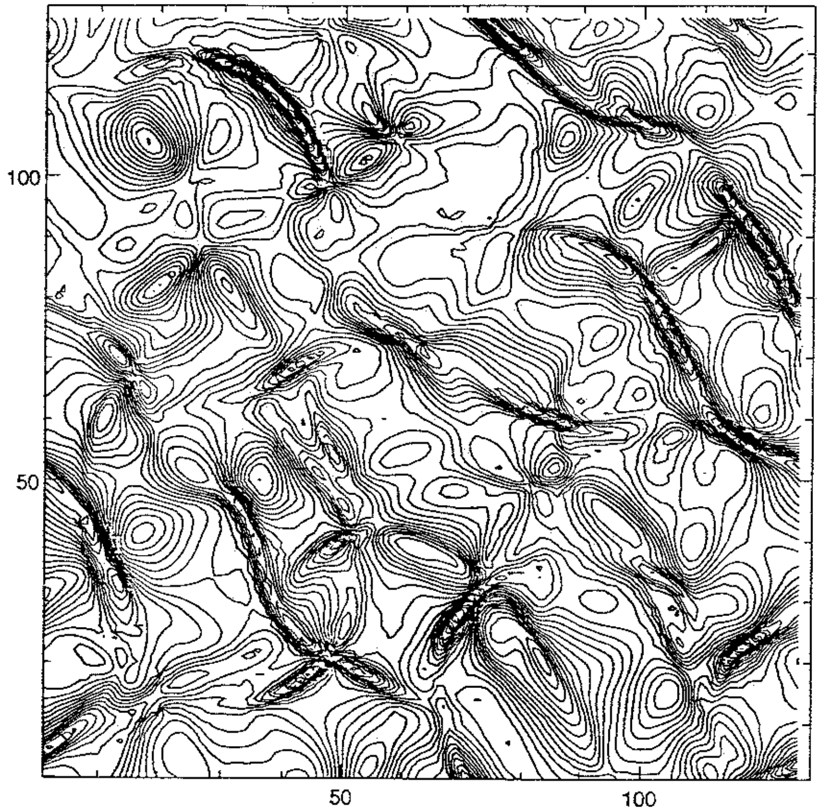

Figure 2.2e : Vorticity Contours from **METS-II** *Scheme at Time-Steps N=50*

contours); probably this comes from the criterion for switching the number of cells to interpolate macroscopic quantities.

The computational time for the **METS** scheme is about 3 second per time step on a **SPARC station 2** for a 128×128 domain, or 15 seconds on a **Cray C-90** for 50 time steps. As pointed out by G. Chudnovsky, if the code were optimized for a Cray, the computational time could probably be reduced to 1.5 seconds for 50 time steps, since he found that just 4% of the computational capacity was used in our calculation on the C-90. Also, as recommended by Shu, we have found the order of our scheme numerically by doing sound wave propagation for successively refined grids, and the order is around 2.

- **Kolmogorov Test Case**

The Kolmogorov test case is taken from a paper about a lattice gas method by P. Kornreich and J. Scalo[20]. We use this shear flow example to illustrate the viscosity effects in the **MET** scheme. Initially the $\widehat{x}$-component of velocity is $u_x = u_0 sin(2\pi y/\mathcal{L})$ with $u_0 = 0.5$ and the $\widehat{y}$-component is $u_y = 0$. Our simulation uses a 64×64 mesh with initial homogeneous mass density $\rho = 1.0$ and thermal energy density $\epsilon_t = 0.67$, where the wavelength $\mathcal{L}$ is 64 and periodic boundary conditions are applied. Since no perturbations are included in the initial data, the Navier-Stokes equations predict that the velocity profile should keep the same shape with $\widehat{x}$-velocity decreasing with time. In order to study viscosity effects quantitatively we have compared the kinetic energy decay rate obtained from the exact solution of the Navier-Stokes equations with the results from the numerical simulation. Since the initial kinetic energy density is around $\epsilon_k \simeq 0.125$ and is substantially less than the thermal energy ($\epsilon_t = 0.67$), we can almost regard pressure, density and temperature as constants and ignore the variation of the dynamic viscosity η in space and time. From the analysis at the end of section(2.2) , we can get an explicit relation between

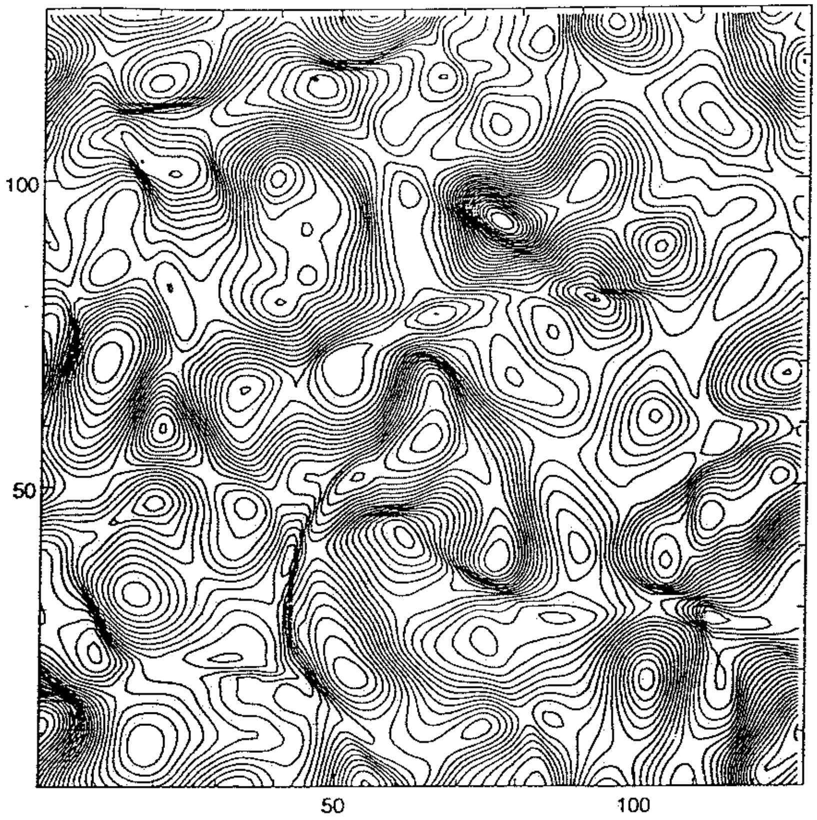

Figure 2.3a : Density Contours from **METS-II** *Scheme at Time-Steps N=90 for Re=150*

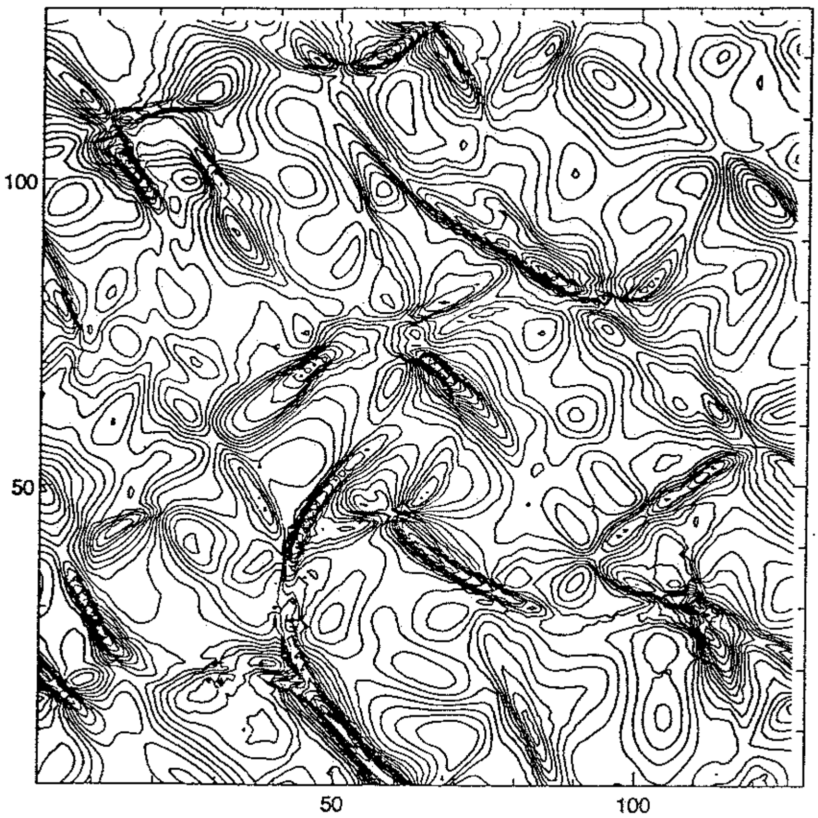

Figure 2.3b : Vorticity Contours from **METS-II** *Scheme at Time-Steps N=90 for Re= 150*

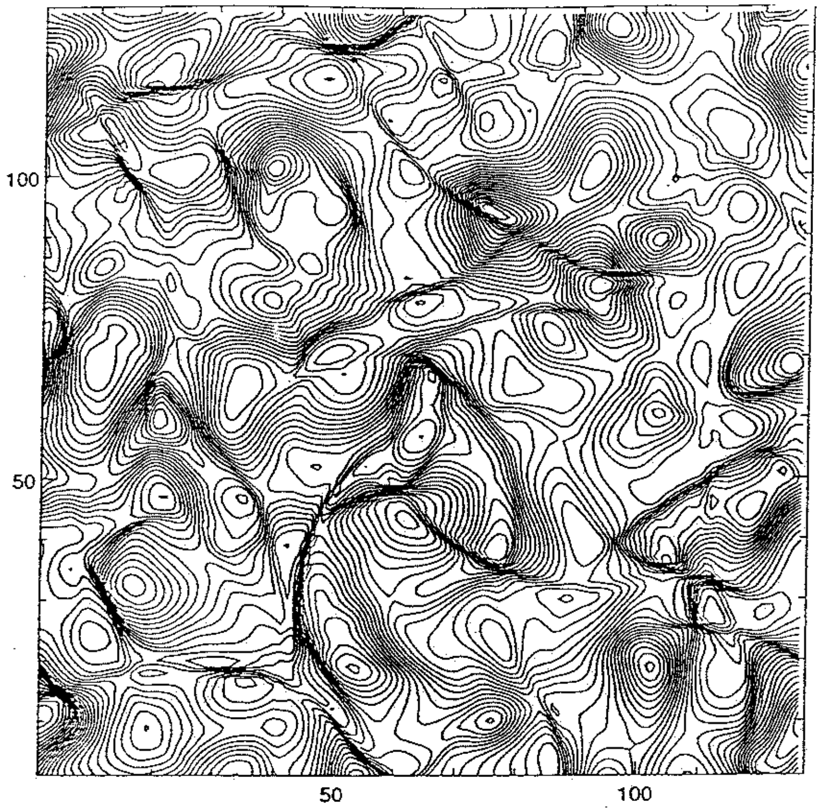

Figure 2.4a : Density Contours from **METS-II** *Scheme at Time-Steps N=90 for Re=1,500*

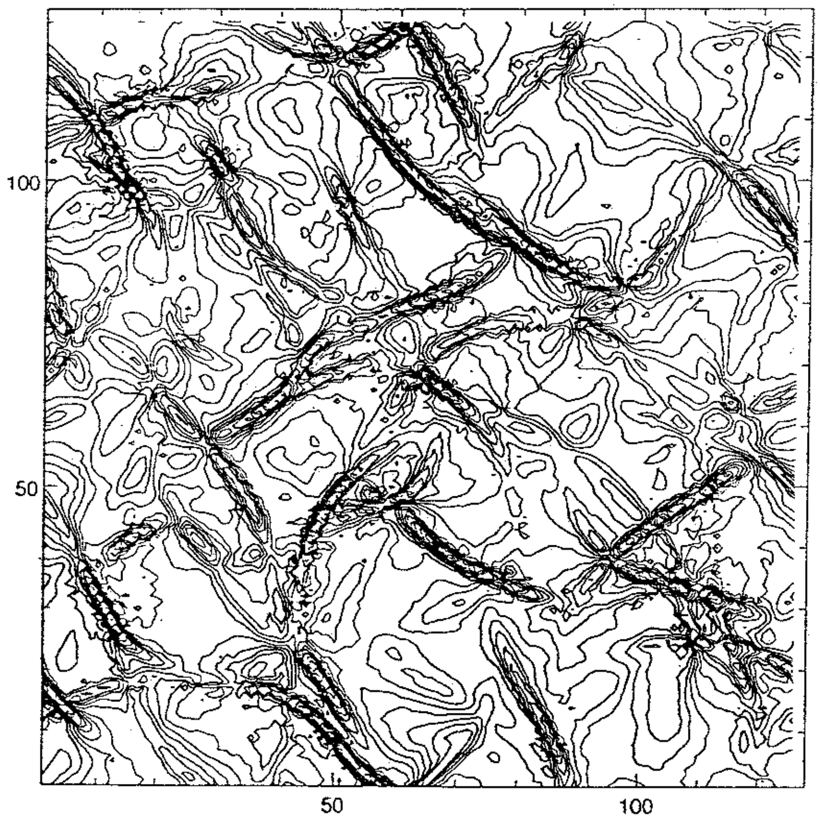

Figure 2.4b : Vorticity Contours from **METS-II** *Scheme at Time-Steps N=90 for Re= 1,500*

η and C_1. By solving the Navier-Stokes equations, the following expression for the theoretical kinetic energy decay rate is obtained:

$$\frac{E(t)}{E(0)} = exp[-C_1(\frac{2\pi}{\mathcal{L}})^2\sqrt{\frac{2p}{\rho^3}}t], \tag{3.4}$$

where t is the time. Using $\frac{E(t)}{E(0)} = e^{-\nu_{NS}t}$ to replace the above equation, we can get the connection between the theoretical viscosity coefficient and C_1:

$$\nu_{NS} = C_1(\frac{2\pi}{\mathcal{L}})^2\sqrt{\frac{2p}{\rho^3}}. \tag{3.5}$$

We have also run this case using our code up to time $t = 1000$ for six different values of the parameter C_1. By fitting our numerical results at $t = 1000$ to $E(t)/E(0) = e^{-\nu_{Exp}t}$, we can calculate the corresponding experimental coefficient ν_{exp}. The following table shows the comparison between the theoretical values and the experimental ones for different C_1 :

Quantitative Viscous Effects		
C_1 Coefficients	ν_{NS}	ν_{exp}
0.01	7.0563×10^{-5}	6.984×10^{-5}
0.03	2.1169×10^{-4}	1.982×10^{-4}
0.05	3.528×10^{-4}	3.134×10^{-4}
0.07	4.939×10^{-4}	4.162×10^{-4}
0.10	7.0563×10^{-4}	5.781×10^{-4}
0.20	1.411×10^{-3}	8.501×10^{-4}

From the above table, it is clear that this code gives numerical solutions of the Navier-Stokes equations in this case, and the difference between the numerical and exact solutions becomes smaller for smaller collision time τ. The deviation of the numerical results from the results of the Navier-Stokes equation becomes obvious with increasing C_1. The reason is that, in this problem, the CFL time step is about $T \sim 0.60$, and the collision time is $\tau = 1.366C_1$. As C_1 increases, the collision time becomes closer to the time step, and we approach the point where the problem should be treated by rarefied gas dynamics; this is beyond the present scope of our code. In order to confirm the exponential kinetic energy decay effect, we also give a plot of $ln(E(t)/E(0))$ as a function of time in Fig.(2.5) ; the slope of the straight line confirms the exponential decay rate.

- **Laminar Boundary Layer**

The laminar boundary layer problem is taken from Allmaras's paper[1]. The flow field evolves above a flat plates (located along the $\widehat{x}$-direction) at zero incidence. The free stream Mach number is $M_\infty = 0.3$ and the Reynolds number is $Re = 500,000$ per unit length. From M_∞ and the mass and momentum densities $\rho = 1.0, P_x = 1.0, P_y = 0.0$, we can first get the sound speed, then the internal energy. After adding the kinetic energy, the initial total energy density is $\epsilon_t = 20.34126984$. Then, from the Reynolds number Re and Eq.(2.16), we find the parameter value $C_1 = 0.0000010030$. The computational domain is a rectangle extending 0.54 units upstream of the leading edge and 1.50 units downstream. The upper boundary is located 0.03 units above the flat plate. The grid is parabolically stretched away from the leading edge in the $\widehat{x}$-direction, symmetrically upstream and downstream of the leading edge. The grid is also stretched parabolically away from the lower boundary in the upward $\widehat{y}$-direction. Two computational domains of 32×16 and 16×8 were used in this boundary layer problem. The no-slip boundary condition is imposed on the flat plate by reversing the velocity direction in cells behind the flat plate. The zero average velocity at the flat plate corresponds to the Navier-Stokes boundary condition. The top and left boundaries keep the initial input flow condition, and the right boundary uses the free-flow condition. In this simulation, because of non-uniformity of the grid sizes, we have used much simpler initial interpolations for the

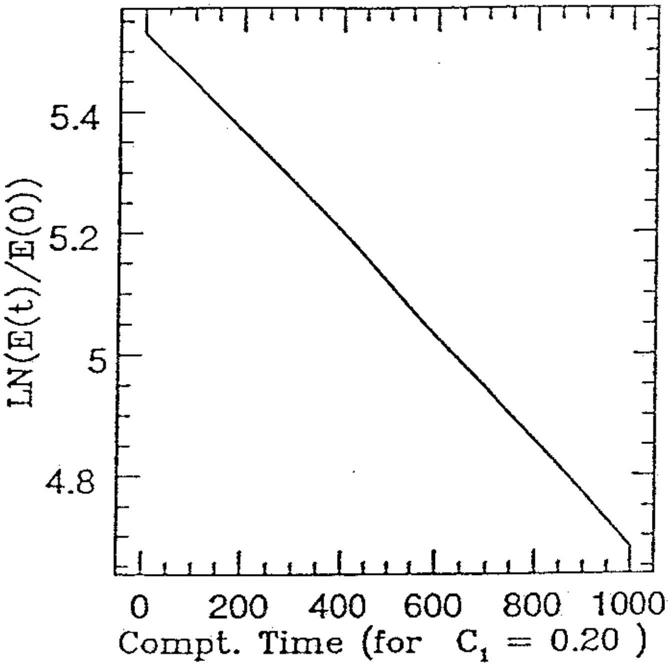

Figure 2.5 : The relation between $ln(\frac{E(t)}{E(0)})$ *and time* t

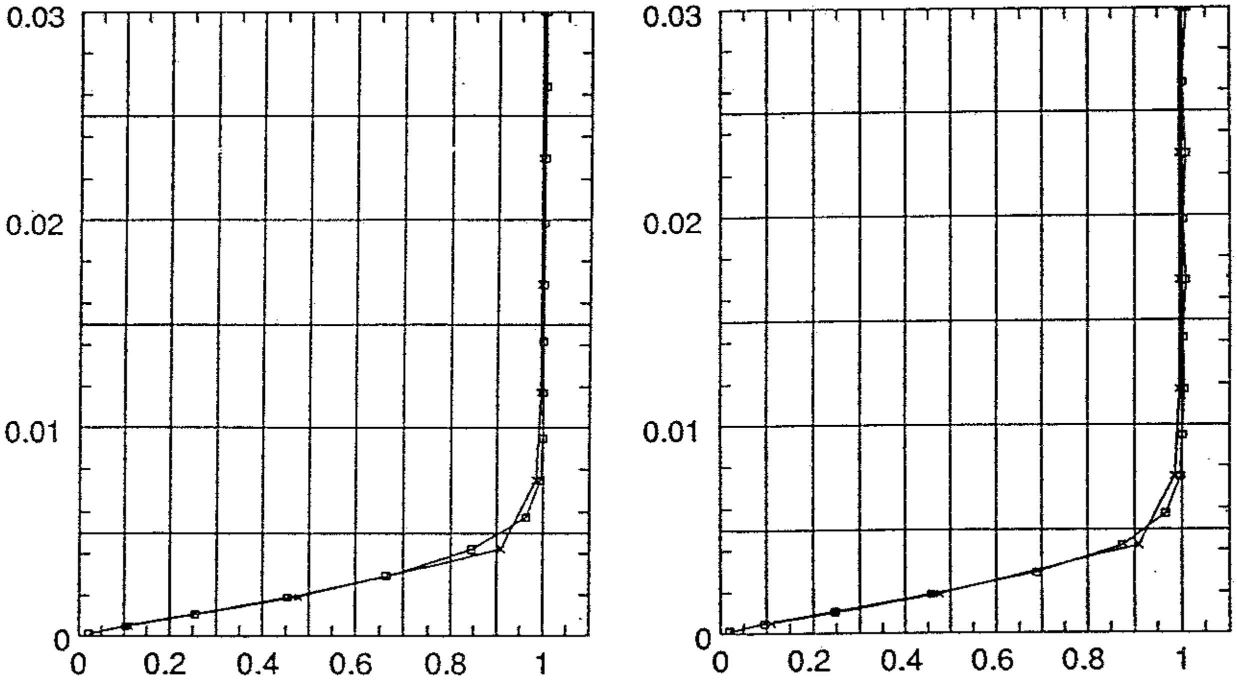

Figure 2.6 : Boundary layer velocity: (R.) **METS-II** *scheme and (L.)* **MET** *scheme*

mass, momentum and energy at the beginning of each time step; for all quantities, we assign the cell average values to the volume center, and use linear interpolations.

The time step is determined by the CFL condition, and the output time is equal to the time needed for the free stream flow to move from the left end of the flat plate to the right end. The final output for the $\widehat{x}$ directional velocity distribution on the line perpendicular to the flat plate is taken at $x \simeq 1.0$, which is close to the mid-point of the plate. The simulation results from the **MET** scheme are shown at the left side of Fig.(2.6), where the curve from our 32 × 16 mesh is almost identical to the correct Navier-Stokes solutions (Allmaras[1]). Even the results from fewer grid points (16 × 8) are very accurate when compared with the results presented in Allmaras' paper. The **METS-II** scheme gives almost the same results, shown on the right side of Fig.(2.6) for the 32 × 16 and 16 × 8 mesh separately.

2.5 Conclusion

In this chapter, we have derived a new numerical Navier-Stokes solver from gas-kinetic theory. The BGK model provides a physical formulation for hydrodynamic problems which is distinct from other methods, *i.e.* from the Euler and Navier-Stokes equations. The combination of the advection and dissipation terms in the integral solution of the BGK model and the inclusion of the linear terms in the initial values of macroscopic quantities make the scheme simpler and more accurate than some of the current high resolution schemes.

Some of the properties and advantages of this numerical gas-kinetic scheme based on the BGK model are the following:

1). For the Euler and Navier-Stokes equations the distribution functions completely disappear in the final codes, which could therefore be written as (highly nonlinear) difference schemes. In common with other Boltzmann-type codes effective upwind differencing is achieved by using the distribution function to weight the information carried by all characteristics through a given point in space. It has often been noted that conventional Boltzmann-type codes have a high degree of arbitrariness in the choice of the distribution function — we have effectively resolved this question by using the BGK model to solve for the evolution of the distribution function in time, and subsequently finding time-dependent fluxes from this solution.

2). In this chapter we have used very simple linear interpolations for all conservative quantities for all test cases; even so, the resolution of the simulation results are pretty high. The reason is that in this scheme we can explicitly follow the time evolution of the gas distribution function from the initial linear interpolation. Here the orders in space and time are the same and consistent with the solution of the BGK model; no middle stages are needed for a high order resolution in time. Usually, Runge-Kutta methods are used for to achieve temporal accuracy in high-resolution hydrocodes.

3). The implicit property in the evaluation of the $\hat{A}$ term in Eq.(2.18) allows this Navier-Stokes scheme to use the CFL condition as the timestep $\delta t = \mathcal{O}(\Delta x)$; otherwise, when the macroscopic Navier-Stokes equations are solved by explicit methods, there is a severe restriction on the timestep $\delta t \simeq \delta x^2/\nu$, where ν is the viscosity coefficient. This is the reason why our time step in the isotropic turbulence case is three times larger than the time step in the Navier-Stokes ENO code. This restriction for the time step in some schemes are usually relaxed by using implicit Runge-Kutta methods, especially for steady state solutions (Jameson *et al* [17]).

4). This scheme includes both $\partial/\partial x$ and $\partial/\partial y$ terms at the same time in the flux evaluations, which is different from directional splitting codes, where just one of them is included. Even in a directional splitting implementation of our code, obtained by deleting $\partial/\partial y$ when calculating $\widehat{x}$ directional fluxes, the $\widehat{y}$-momentum flux can still be saved and found explicitly in the $\widehat{x}$-direction. This is different from some

Godunov-type schemes for two dimensional simulations, where the $\hat{y}$-momentum flux is evaluated separately. Actually, accuracy in handling the $\hat{y}$-momentum is critical for the calculation of one-dimensional shear flows, such as the Rayleigh Problem(Chu [9]).

5). Since all trajectories (characteristics) of individual particles are followed in two dimensional space, this gives an intrinsically multidimensional aspect to the evolution stage. Indeed, for a multidimensional scheme, the reconstruction stage also needs to be multidimensional. One way of doing this is to identify the initial discontinuity direction and then expand all quantities relative to the discontinuity surface. In any case, the multidimensional evolution in our gas-kinetic scheme makes it different from multidimensional schemes which start from Euler or Navier-Stokes equations directly, where local decompositions into waves along a certain number of characteristic are used (Rumsey *et al.* [33]). These schemes also have initial interpolation problems, and there are also unsolved questions concerning the evolution of individual waves.

6). It would not be hard to include second and third order terms in the Taylor expansions for g and f , such as $\partial^2/\partial x \partial y$ and $\partial^2/\partial x \partial t$, and their coefficients can be explicitly evaluated using derivatives of the conservation constraints $< f - g >= 0$. However, this would make the code not only more sensitive to the precise form of the initial interpolation, but also greatly increase the computational time.

7). There are still some options available to improve our scheme by incorporating smoother nonlinear limiters in the interpolations. The noise in the vorticity contours of the Isotropic Turbulence test case at high Reynolds number is probably due to a lack of smooth behavior of the limiters we used.